npj | quantum information

Article

Published in partnership with The University of New South Wales

https://doi.org/10.1038/s41534-024-00852-7

Mapping of valley splitting by conveyor-mode spin-coherent electron shuttling

Check for updates

Mats Volmer[1,5], Tom Struck[1,2,5], Arnau Sala[1], Bingjie Chen[1], Max Oberländer[1], Tobias Offermann[1], Ran Xue[1], Lino Visser[1], Jhih-Sian Tu[3], Stefan Trellenkamp[3], Łukasz Cywiński[4], Hendrik Bluhm[1,2] & Lars R. Schreiber[1,2]

In Si/SiGe heterostructures, the low-lying excited valley state seriously limits the operability and scalability of electron spin qubits. For characterizing and understanding the local variations in valley splitting, fast probing methods with high spatial and energy resolution are lacking. Leveraging the spatial control granted by conveyor-mode spin-coherent electron shuttling, we introduce a method for two-dimensional mapping of the local valley splitting by detecting magnetic field-dependent anticrossings of ground and excited valley states using entangled electron spin-pairs as a probe. The method has sub-μeV energy accuracy and a nanometer lateral resolution. The histogram of valley splittings spanning a large area of 210 nm by 18 nm matches well with statistics obtained by the established but time-consuming magnetospectroscopy method. For the specific heterostructure, we find a nearly Gaussian distribution of valley splittings and a correlation length similar to the quantum dot size. Our mapping method may become a valuable tool for engineering Si/SiGe heterostructures for scalable quantum computing.

Si/SiGe heterostructures are one of the most promising host materials for spin qubits[1], as they offer low potential fluctuations, charge noise, long coherence times[2], high-fidelity control[3–6] and are industry-compatible platforms that allow for fabrication in established silicon production lines[7]. However, some devices exhibit low-lying valley states that limit high-temperature operation of spin-initialization, -manipulation, and Pauli-spin blockade readout, and hinder spin-shuttling[8–11]. Local minima in the energy splitting between the low-lying valley states, E_{VS}, pose the main obstacle to the scalability of this platform. Innovations in growth and fabrication strategies[12–14], but also efficient methods to benchmark the local valley splitting are needed to overcome it.

A large range of local E_{VS}, from 6 μeV to >200 μeV, was observed in gate-defined quantum dots (QDs) formed in Si/SiGe heterostructures[8,15–26]. The E_{VS} is theorized to be a randomly distributed local material parameter, subject to atomic-scale crystal variations[12,27–31] of the Si/SiGe heterostructure. Thus a few measurements of E_{VS} at different spots do not suffice to confidently benchmark the quality of a heterostructure[31]. Many different methods to determine the E_{VS} of a Si/SiGe QD were reported, such as thermal excitation[8], pulsed-gate spectroscopy in a single[21,24] or double[23] QD, spin funnel measurement in two exchange-coupled QDs[32,33] and the identification of the spin-valley relaxation hot-spot[20,21]. Other methods measure the singlet-triplet energy splitting E_{ST}, being a lower bound of the E_{VS}, by Pauli-spin blockade[19] or magnetospectroscopy[15–17,22,26,31]. High-energy resolution has been achieved by dispersive coupling, to a resonator[18,34], and some attempts towards laterally mapping E_{VS}[21,24,25] have been published, but these are involved, time-consuming, and cover a small area. Determining E_{VS} by Shubnikov-de-Haas oscillations[35] grants information on the out-of-plane electric field dependence of E_{VS}[36], but lacks lateral resolution and tends to overestimate E_{VS} due to localization by the out-of-plane magnetic field[37]. To this end, we need a time-efficient method with good energy resolution that can map the valley-splitting landscape of a realistic Si/SiGe quantum chip.

In this work, we present an efficient method for mapping the local valley splitting in silicon across a large area with a resolution that can capture the local variations of E_{VS}. We employ singlet-triplet oscillations of a spatially separated pair of spin-entangled electrons, with one of them shuttled to a distant position as a probe to locally detect magnetic field-induced anticrossings between spin-valley states, from which we then obtain a magnitude for E_{VS}[38]. Leveraging coherent conveyor-mode shuttling[11,39–41], we extend this analysis to create a dense one-dimensional map of the valley splitting for a Spin-Qubit-Shuttle (SQS)[11,41,42]. Our method yields a nanometer resolution along the shuttle direction, which suffices to resolve local

---

[1]JARA-FIT Institute for Quantum Information, Forschungszentrum Jülich GmbH and RWTH Aachen University, Aachen, Germany. [2]ARQUE Systems GmbH, 52074 Aachen, Germany. [3]Helmholtz Nano Facility (HNF), Forschungszentrum Jülich, Jülich, Germany. [4]Institute of Physics, Polish Academy of Sciences, Warsaw, Poland. [5]These authors contributed equally: Mats Volmer, Tom Struck. ✉e-mail: lars.schreiber@physik.rwth-aachen.de

features in the valley-splitting landscape depending on the QD size. By applying voltage offsets to two long gates parallel to the shuttle direction, the shuttle trajectory can be displaced (here up to 18 nm), which results in a two-dimensional map of E_{VS}. We thus present four valley splitting traces, each with an approximate length of 210 nm, with 150 E_{VS} measurements per trace and a sub- μeV energy uncertainty. The position of the electron in the one-dimensional electron channel (1DEC) is derived from the ideal shuttling potential without taking disturbance of electrostatic disorder into account. Specifically, short-range tunneling of the electron across disorder-induced barriers cannot be fully excluded. We report measured values of the valley splitting that range from 4.6 μeV to 59.9 μeV, and that exhibit a continuous behavior punctuated by sudden jumps. We attribute these rapid changes to unintentional tunneling events during conveyor-mode shuttling, which we can mitigate by displacing the channel vertically. Our method enables efficient valley-splitting mapping, which provides sufficient statistics to infer an accurate mean and shape of the distribution by single-electron spin shuttling. In this study, the main limitation is the charge shuttle distance at high velocity. Disorder and limited confinement strength due to attenuation on the high-frequency lines hinders shuttling past 210 nm.

The device used for the experiments is the same as that described in ref. 41. It comprises three Ti/Pt gate layers, separated by 7.7 nm thick Al_2O_3, and is fabricated on an undoped $Si/Si_{0.7}Ge_{0.3}$ quantum well (see method section for layer stack). The 1DEC is formed by an ~1.2 μm-long split-gate with 200 nm spacing (shown in purple in Fig. 1a). By applying DC voltages V_{ST}, V_{SB} to the split-gate, the 1DEC is confined in y direction. Seventeen clavier gates are fabricated on top of the device, with a combined gate pitch of 70 nm. Of these, eight are on the second metal-layer and labeled G2, G16, 3 × S1, and 3 × S3, while nine are on the third metal-layer and labeled G1, G3, G15, G17, 3 × S2, and 2 × S4. In conveyor mode[11], two to three clavier gates are electrically connected to four so-called shuttle gates S1, S2, S3, and S4[40,41,43]. The shuttle gates are named differently, as each shuttle gate comprises more than one clavier gate as indicated in Fig. 1a. As a result, every fourth clavier gate shares the same potential, which leads to a periodic electrostatic potential with a period of $\lambda = 280$ nm. Generating a traveling wave potential (see methods section for details on electron shuttling in conveyor mode), we coherently shuttle the electron spin for a nominal distance of up to 336 nm in a global in-plane magnetic field B. We shuttle at a frequency of 10 MHz, which corresponds to an electron velocity of 2.8 ms^{-1}. The SQS has a single-electron transistor (SET) at each end, serving as electron reservoir and proximity charge sensors.

Results

DQD valley-splitting measurement

As a basis for the E_{VS} mapping technique discussed later, we first consider a method to determine E_{VS} in a static double quantum dot (DQD). Therefore, next to the left SET, we form a DQD under gate G2 and the leftmost clavier gate from S1. Gates G1, G3, and the leftmost clavier gate of S2 act as barrier gates. Figure 1b displays a charge stability diagram for the DQD. We measure the valley splittings E_l (E_r) of the left (right) QD of the DQD using singlet-triplet oscillations, which probe the magnetic anticrossings induced by spin-valley couplings in each QD.

To this end, we apply the following pulse sequence: We load four electrons into the leftmost QD for 1 ms to initialize into a spin-singlet (S) state in the (4,0) charge state[41] (Fig. 1b, stage I). Next, we split the spin-singlet by rapidly pulsing to the (3,1) charge state (stages I→S) within a rise-time of ≈1.2 ns (limited by 300 MHz bandwidth of our waveform generator). As a function of wait-time τ_{DQD}, singlet-triplet oscillations occur with a frequency ν proportional to B, and the difference of the electron g-factors Δg of the DQD. For detection of the S-state, we pulse into the Pauli-Spin-blockade (PSB) (area between red dashed lines in Fig. 1b) and wait for 500 ns. The PSB charge state is read out by the SET current I_{SET}, after freezing this charge state by reducing the DQD tunnel-coupling (stages P→F; $V_{G3}(F) \approx 0.7$ V)[44]. There, we read the charge state via measuring I_{SET} for 1 ms. We repeat this pulse sequence (Fig. 2a) while varying τ_{DQD} from 0 to 1.5 μs, in 100 equidistant time steps. Repeating this loop 1000 times, we calculate the spin-singlet return probability $P_S(\tau_{DQD})$ at a set B (Fig. 2b), while every 10 loop iterations the correct electron filling of the DQD is reinitialized as a precaution. In order to counter slow noise-related drifts on the PSB and the SET, both the PSB-stage voltage as well as the SET voltages are retuned after 1000 loop-iterations (details in the methods section).

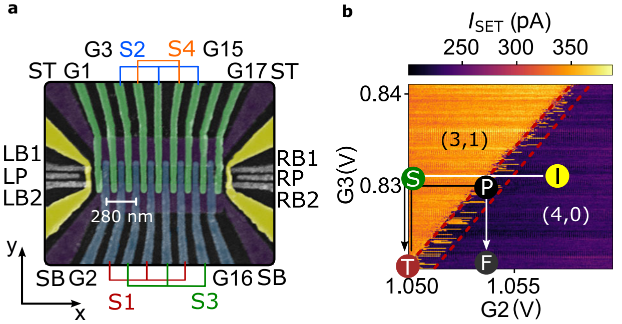

Fig. 1 | Spin-Qubit shuttle (SQS) device and experimental method. a False-colored scanning electron micrograph (SEM) of the device used in the experiment, showing a top-view on the three metallic layers (1st purple, 2nd blue, 3rd green) of the SQS, and their electrical connection scheme. At both ends, single-electron transistors (SETs) are formed in the quantum well by gates LB1, LB2, and LP (RB1, RB2, and RP, respectively) on the second gate layer, with the current path induced by the yellow gates on the third layer. Scale bar corresponds to 280 nm. **b** Charge stability diagram of the outermost left DQD recorded by the left SET current I_{SET}. DQD fillings are indicated by (n, m), with n and m denoting the number of electrons in the left and right QDs, respectively. The red dashed lines indicate the boundaries of the PSB region. Labeled circles indicate voltages on G2 and G3 and correspond to pulse stages used in subsequent experiments. Arrows indicate pulse order. Pulse stages T as well as F reach down to $V_{G3} = 0.7$ V.

The singlet-triplet oscillation frequency ν contains the important information and is extracted as follows. We fit the measured $P_S(\tau_{DQD}, B)$ line by line to

$$P_S(\tau_{DQD}) = a\exp\left(-\frac{\tau_{DQD}^2}{T_2^{*2}}\right)\cos\left(2\pi\nu\tau_{DQD}+\varphi\right)+c, \tag{1}$$

where a, ν, φ are the visibility, frequency, and phase of the spin-singlet-triplet oscillations, respectively, and T_2^* is the ensemble spin-dephasing time of the entangled spin-state. The offset c is partly absorbed by subtraction of the linewise mean $\langle P_S(\tau_{DQD})\rangle$. The fit with a Gaussian decay (Fig. 2c) captures all the relevant features of the measured data (cf. Fig. 2b). Here, we are interested in $\nu(B)$ (black dots in (Fig. 2d)), which reveals two distinct anticrossings on top of a constant slope p. The slope is expected to be proportional to $\Delta g = \frac{ph}{\mu_B}$ (with h and μ_B Planck's constant and Bohr-magneton, respectively) provided the effective magnetic field gradient due to Δg exceeds the Overhauser field gradient (~0.01 mT) of the randomly fluctuating ^{29}Si and ^{73}Ge nuclear spin-baths. As this condition is easily fulfilled, we can fit Δg (Table 1).

Next, we argue that the two anticrossings stem from the spin-valley coupling in each of the QDs, and can be employed as a precise probe for the valley splittings E_l and E_r. As we will show in the following sections, this anticrossing is crucial for mapping the valley splitting by coherent spin shuttling. We consider spin-conserving tunneling only, and assume that intervalley tunneling couples higher energy valley, $|+\rangle$, in the left QD to the lower energy valley, $|-\rangle$ in the right QD, so that charge separation (4, 0)→(3, 1) creates a state in which two electrons form a spin-singlet in the $|-\rangle$ valley in the left QD[33,45], while the remaining two electrons form a spin-singlet $|S^{+-}\rangle = (|\uparrow\downarrow +-\rangle - |\downarrow\uparrow +-\rangle)/\sqrt{2}$, where the first (second) arrow and sign indicate the spin and valley state of the electrons in the singly-occupied valleys of the left (right) QD. This $|S^{+-}\rangle$ is coupled to the unpolarized triplet $|T_0^{+-}\rangle = (|\uparrow\downarrow +-\rangle + |\downarrow\uparrow +-\rangle)/\sqrt{2}$ by the difference between the Zeeman energies of the two

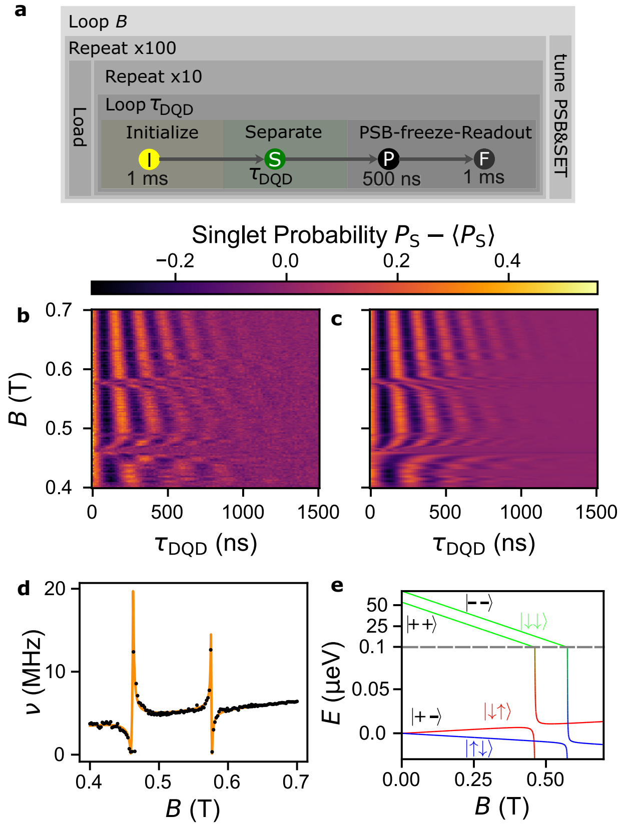

Fig. 2 | Spin-valley anticrossing in a DQD. a Experiment flowchart explaining the microscopic pulse stages, parameter loops as well as stabilizing measures. Waiting times at pulse stages are indicated by times below. **b** Normalized singlet return probability as a function of the magnetic field B and DQD separation time τ_{DQD}. The singlet return probability P_S is normalized such that each horizontal line averages to zero. **c** Fit to the data from **b** using Eq. (1). **d** Frequencies extracted from the fit in **c**. The orange curve is a least-square fit to the data. Uncertainties of frequencies are on the order of 100 kHz and smaller than the size of the black dots. **e** Energy spectrum of the Hamiltonian from Eq. (2). The color mixture represents the spin-state composed from colors of labeled spin base state, while the black symbols label the valley state. For clarity, the energy axis is upscaled around the $|\uparrow\downarrow +-\rangle$ and $|\downarrow\uparrow +-\rangle$ states with spin projection along the z axis $m_s = 0$. For these states, their magnetic field dependence, proportional to $\Delta g \mu_B$, is four orders of magnitude smaller than that of the states $|\downarrow\downarrow --\rangle$ and $|\downarrow\downarrow ++\rangle$, with $m_s = -1$. The parameters used in **e** are extracted from the fit in **d**.

Table 1 | Fit results of the spin-valley anticrossing in a DQD

Parameter	value	1σ	unit/factor	coupling states
Δg	6.58	0.04	10^{-4}	-
E_r	53.52	0.17	μeV	-
E_l	66.64	0.04	μeV	-
ν_r	82	14	neV	$\lvert\downarrow\uparrow +-\rangle$ & $\lvert\downarrow\downarrow ++\rangle$
ν_l	58	3	neV	$\lvert\uparrow\downarrow +-\rangle$ & $\lvert\downarrow\downarrow --\rangle$

Fit parameters, together with their uncertainty, for the model presented in Eq. (2), using the data from Fig. 2c, e. For the coupling elements ν_r and ν_l, we also indicate the states that are coupled.

electrons with opposite spin in different valley states, $\Delta E_Z = \mu_B B(g_{r,-} - g_{l,+})$, which results from the g-factor difference between an electron in the right QD and $|-\rangle$ valley (with g-factor $g_{r,-}$) and an electron in the left QD and $|+\rangle$ valley (with g-factor $g_{l,+}$). Spin-valley interaction in the right QD couples $|S^{+-}\rangle$ and $|T_0^{+-}\rangle$ to states in which the electron in this QD occupies the $|+\rangle$ valley, and the spins of the two electrons in singly-occupied valley states are aligned, i.e. $|\downarrow\downarrow ++\rangle$ and $|\uparrow\uparrow ++\rangle$. Spin-valley interaction in the left QD couples $|S^{+-}\rangle$ and $|T_0^{+-}\rangle$ to states in which the $|-\rangle$ valley in the left QD is occupied by a single electron having its spin aligned with the electron in the right QD, i.e. $|\downarrow\downarrow --\rangle$ and $|\uparrow\uparrow --\rangle$.

Deep in the (3, 1) regime the dynamics in the relevant space of four lowest-energy states is modeled with a Hamiltonian[38]

$$H = \begin{pmatrix} -\Delta E_Z/2 & 0 & 0 & \nu_l \\ 0 & \Delta E_Z/2 & \nu_r & 0 \\ 0 & \nu_r & E_r - \bar{E}_{Z,+} & 0 \\ \nu_l & 0 & 0 & E_l - \bar{E}_{Z,-} \end{pmatrix} \tag{2}$$

written in the basis of $\{|\uparrow\downarrow +-\rangle, |\downarrow\uparrow +-\rangle, |\downarrow\downarrow ++\rangle, |\downarrow\downarrow --\rangle\}$, where $\bar{E}_{Z,+}$ ($\bar{E}_{Z,-}$) is the Zeeman energy for two electrons with parallel spins in the $|++\rangle$ ($|--\rangle$) states, and ν_l (ν_r) is the spin-valley coupling in the left (right) QD. Note that spin-valley mixing with $|\uparrow\uparrow\rangle$ states can be safely neglected as $\nu_{l(r)} \ll E_{l(r)} + \bar{E}_{Z,\pm}$. Fits of data with a model involving also (4, 0) state, and tunnel coupling, t_c, in the DQD, confirmed that t_c has negligible effect on spin dynamics in (3, 1) regime. As explained above, the Overhauser field is disregarded.

We diagonalize the Hamiltonian and fit $\nu(B)$ in Fig. 2d (orange line) with parameters shown in Table 1 corresponding to the energy spectrum shown in Fig. 2e. Note that the assignment of the anticrossings to the left and right QDs is arbitrary at this stage of the analysis; the indices l and r in Table 1 can be swapped. Our model fits $\nu(B)$ very well. Hence, the occurrence of spin-valley anticrossings does not require any tunnel-coupling in the DQD except from initialization and detection of the S-state. This notion is decisive for valley mapping by shuttling, which involves separation of the two electrons. Assignment for the valley splitting is straightforward: the magnetic field B_{VS} in the center of the anticrossing can be converted to a E_{VS} by $B_{\mathrm{VS}} = E_{\mathrm{VS}}\mu_B/g$, where $g = 2$ and the width of the anticrossing is proportional to the coupling strength ν. Here, we omit the g-factor variation as Δg is less than 0.1 % of g and thus gives an error of less than 0.1 % on the detected E_{VS}. A similar analysis of a DQD formed at different screening gate voltages can be found in Supplementary Fig. 1. Furthermore, note that the valley splitting measured for the left QD is the three-electron valley splitting.

Valley-splitting mapping

Next, we discuss the use of spin-valley anticrossing in a QD for mapping the valley splitting along the 1DEC. Therefore, in addition to the pulse scheme explained above (Fig. 2a), we shuttle the electron spin in the right QD fast by a distance $d(\tau_S)$ (for shuttle time τ_S, see Eq. (6) in the method section), let the entangled singlet-triplet-state evolve for a fixed waiting period ($\tau_w = 300$ ns) and then shuttle it back by the same distance for PSB detection. Thus, the pulse scheme for mapping (Fig. 3a) is complemented by the 10 ns long stage T (voltages in Fig. 1b), a shuttle pulse for time τ_S, a fixed waiting period at stage d, the time-reversed shuttle pulse to enter stage T (DQD with large barrier) followed by stage S, the detuned tunnel-coupled DQD in charge state (3,1). Note that compared to the pulse scheme (Fig. 2a), we measure $P_S(d, B)$ instead of $P_S(\tau_{\mathrm{DQD}}, B)$, which turns out to be sufficient for mapping the valley splitting. Another parameter that can be varied is τ_w in stage d. Measurements of the three-dimensional parameter space $P_S(d, \tau_w, B)$ are shown in Supplementary Fig. 2. A scan $P_S(d, \tau_w, B = 800\ \mathrm{mT})$ is employed to probe $\nu(d)$ fitted by Eq. (1) with τ_w replacing τ_{DQD} (Fig. 3b). Notably, the fitted frequency of the singlet-triplet oscillations $\nu(d)$ varies smoothly, with exception at $d \approx 120$ nm, and drops close to zero at some d_i (black arrows). Presumably, $\nu(d)$ is governed mainly by variations of the electron g-factor in the propagating QD due to variations in confinement. These are expected partly due to the deterministic breathing of the confinement potential of the moving QD, partly due to electrostatic disorder in the quantum well[11]. Note that we cannot distinguish by measurement of $\nu(d)$, which of the QDs has the larger electron g-factor.

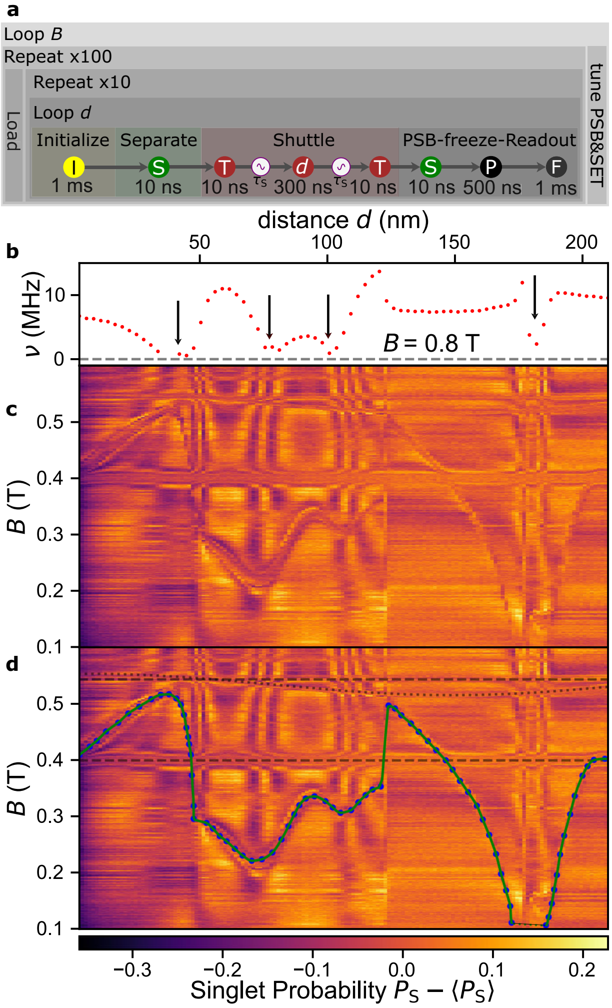

Fig. 3 | Mapping of the local valley splitting using the ST$_0$ oscillations. **a** Flowchart of the microscopic pulse stages, parameter loops as well as stabilizing measures. Waiting times at pulse stages are indicated below. Compared to Fig. 2a, the electron is shuttled by a distance d, waits there for $\tau_W = 300$ ns and is shuttled back, prior to PSB. **b** Extracted frequencies $\nu(d)$ measured at a magnetic field of 0.8 T. The 1σ-intervals are smaller than the symbols. **c** Raw data of the singlet return probability P_S as a function of shuttle-distance d and magnetic field B. To enhance contrast, we subtract the averaged return probability $\langle P_S \rangle$ for each B. **d** same as **c** with additional markers (see text). The spin-valley anticrossing of the shuttled QD is indicated by blue points connected by a green spline curve.

The local variations of the g-factor difference help us to understand features in $P_S(d, B)$ (Fig. 3c), our main result. Curved (spaghetti-like) features are clearly visible on top of the background that appears when changes of $P_S(d, B)$ along a certain direction in the (d, B) plane are much larger than changes along the corresponding perpendicular direction. For example, at distances d_i (highlighted by arrows in Fig. 3b), at which $\nu(d)$ approaches zero, the P_S signal weakly depends on B, while it depends strongly on d (due to strong variation of $\nu(d)$, see Fig. 3b), resulting in the appearance of vertical features. Besides some horizontal features (marked by black dashed lines in Fig. 3d), which we explain below, there is a continuous widely varying feature marked by the green solid line in Fig. 3d (details in Supplementary Note V). This line follows the spin-valley anticrossing of the shuttled electron spin. It is generated by waiting at d for $\tau_w = 300$ ns and accumulating phase due to a relatively large modification of the singlet-triplet oscillation frequency at the anticrossing. It is thus a measure of $E_{VS}(d)$ along the 1DEC. We support this notion by the $P_S(d, \tau_w, B)$ data shown in Supplementary Note IV.

Notably, at $d = 0$ nm and $B \approx 0.4$ T, this line overlaps with a horizontal feature (marked by the lower dashed line in Fig. 3d), and the B-field matches with one of the E_{VS} of the DQD. This d-independent feature originates from the accumulation of a phase during the stages S and T, at which the DQD in charge state (3,1) is formed. There, the total waiting period is 40 ns (Fig. 3a), which is sufficient to identify the anticrossing by the singlet-triplet oscillations (cf. Fig. 2b). Presumably, this horizontal line is broadened in B as the QD position is slightly displaced in stage T compared to stage S, altering the B at which the anticrossing occurs. Now, it is justified to attribute this anticrossing to the right QD. The index of E_r in Table 1 is, therefore, correct.

The counterpart of the lower horizontal line is the upper horizontal line at $B = 0.54$ T, which matches E_l in Table 1. At its origin ($d = 0$ nm), a wavy feature (black dotted line in Fig. 3d) around the upper dashed line is barely visible. We assign this line to the spin-valley anticrossing of the left (static) QD, due to which a phase is accumulated during $\tau_w = 300$ ns. This is expected, since the sinusoidal voltages applied to the shuttle gates capacitively cross-couple to the left QD. Hence, the left QD is slightly displaced by the same period as the period of the shuttle voltages, and thus its valley splitting gets a tiny d-dependence with this period. This matches exactly the observation in Fig. 3c, d.

Hence, we could explain the features in Fig. 3c, and found striking evidence that the green solid line in Fig. 3d maps the $E_{VS}(d)$ along the 1DEC. The position along B of this line can be resolved with a precision of less than 1 μeV (see Supplementary Fig. 4). Care must be taken to interpret the plotted distance d in terms of a precise location. $d(\tau_S)$ is extracted from the phase of the sinusoidal driving signal (Eq. (6) in the method section). The traveling wave potential exhibits higher harmonics which leads to slight breathing and wobbling of the propagating QD, thus the QD velocity is not exactly constant. Slight variations in the velocity due to potential disorder from charged defects at the oxide interface are of the same order of magnitude[11] imposing an uncertainty on QD position d. We note that we can shuttle the electron forth and back by a maximal one-way distance of $d = 336$ nm, equivalent to 1.2 λ. By reducing the shuttle velocity by a factor of five, we can shuttle the charge forth and back at least 2.0 λ ($d = 480$ nm). This points to a potential disorder peak at $d \approx 340$ nm, which the electron cannot pass at the higher velocity. Here, we limit our mapping range to $d = 210$ nm (extended range shown in Supplementary Note V) to stay far away from this potential disorder peak, but also note that the abrupt change of ν and E_{VS} at $d \approx 120$ nm in Fig. 3b, d indicates some tunneling occurring during the conveyor-mode shuttle process.

2D valley splitting map

For simplicity, we approximate d as the location of the QD now. In order to extend the mapping to the perpendicular direction, we change the screening gate voltages—from $V_{ST} = V_{SB} = 100$ mV while keeping the sum constant—in order to displace the 1DEC in the y direction. Figure 4a displays the extracted splines corresponding to four different screening gate configurations where the nominal displacement in y direction is indicated by colored labels. These distances are calculated by linearly converting the voltage difference $V_{ST} - V_{SB}$ into y displacement with a factor of 6 nm/100 mV (see Supplementary Fig. 7e). The splines are sampled at the measurement resolution of one point per nominal 1.4 nm. For some d marked by dotted lines in Fig. 4a (red trace: ~180–190 nm, violet trace: ~170–185 nm, blue trace: ~110–125 nm), we were unable to identify the E_{VS}, probably because it was below the B-scan range.

Using all this data, we obtain a two-dimensional map of E_{VS} by linear interpolation (Fig. 4b). The overall E_{VS} values are in the lower range of values found in the literature. The important point is, however, that our shuttling-based mapping method gives us an insight into the lateral E_{VS} distribution in our SQS device. There are regions of nearly zero E_{VS} (e.g., $d \approx 180$ nm and $y = -12$ nm), but strikingly they can be avoided by displacing the QD along the y direction (e.g., $y = 6$ nm). This is important for shaping a static QD containing a spin-qubit at a position, at which E_{VS} is sufficiently large and qubit control is feasible. For conveyor-mode shuttling of spin qubits, it allows finding a trajectory of the moving QD, which avoids low E_{VS} spots causing qubit decoherence. Similarly, tunneling of the moving QD across electrostatic disorder barriers (e.g., at $d \approx 125$ nm and $y = 6$ nm) can be avoided by changing the y-displacement (e.g., $y = -12$ nm). The reason for the tuneability of E_{VS} is its short correlation length.

We calculate the correlation coefficient of the set of E_{VS} pairs (without regions of undefined E_{VS}) separated by a geometric distance D as a function of D in Fig. 4c. Additionally, we fit a Gaussian curve as derived from ref. 12.

$$\mathrm{Corr}(D) = \exp\left(-\frac{1}{4-\pi}\frac{D^2}{a_{\mathrm{dot}}^2}\right), \qquad (3)$$

which takes atomistic alloy disorder in the SiGe barrier into account. Here, the fitting parameter $a_{\mathrm{dot}} = \hbar/\sqrt{m_t E_{\mathrm{orb}}}$ is the characteristic QD size, m_t is the transversal effective electron mass in silicon, and E_{orb} is the orbital energy of the electron, assuming a harmonic confinement potential. The fit results in a QD size of a_{dot} ~16 nm, corresponding to E_{orb} ~1.6 meV being on the expected order of magnitude according to electrostatic simulations. Note that the correlation crosses zero and only vaguely follows a Gaussian decay, which is an effect of the limited scan area of the E_{VS} map (correlations of subsets of the data are discussed in Supplementary Note IV). In addition, due to electrostatic disorder E_{orb} is not constant, though assumed to be such in derivation of Eq. (3).

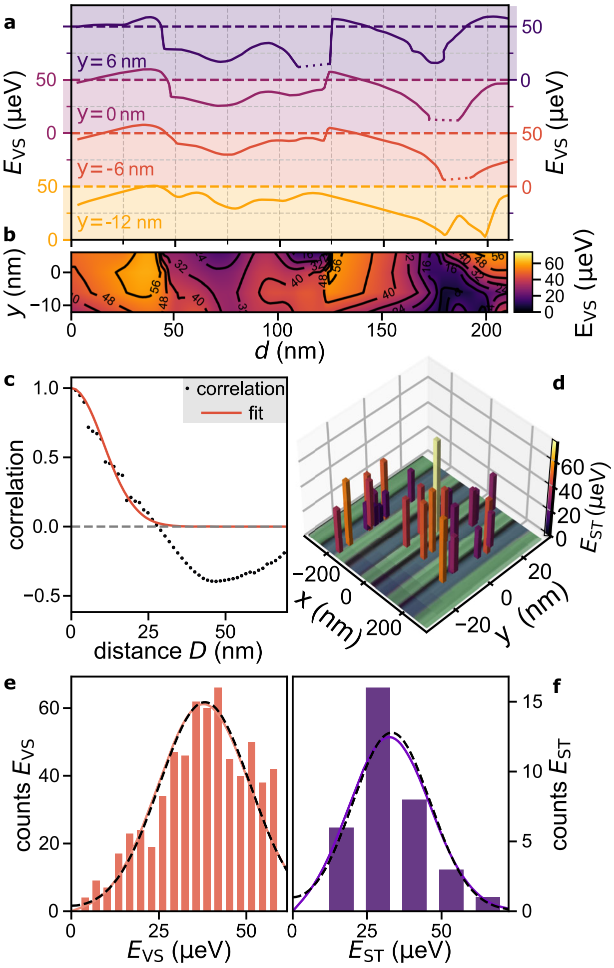

Fig. 4 | Comparison of valley splitting mapping techniques. a Four E_{VS} scan-lines of valley splitting along different y displacements measured by the same method as the data shown in Fig. 3 with the curve at $y = 0$ nm being taken from its panel **d**. Note that each E_{VS} scan-line has its own color-coded energy axis. Dashed parts on the valley splitting traces indicate areas in which an anticrossing was not observable or out-of B range. **b** False-color 2D map of E_{VS} exclusively based on the data shown in **a**. **c** Correlation coefficient (dots) of the set of measured E_{VS} pairs separated by a geometric distance $D = \sqrt{\Delta y^2 + \Delta d^2}$, as a function of D, exclusively based on the data shown in **a**. A Gaussian least-square fit to the correlation for $D < 28$ nm is included as a red solid line. **d** 2D map of E_{ST} values obtained on the same wafer, but different device employing magnetospectroscopy. E_{ST} values are shown on the vertical axis as well as by the color of each bar. Green-blue stripes are the colored scanning electron micrograph of the clavier gates of the used device (cf. Fig. 1a). **e** Histogram of the measured E_{VS} obtained by equidistant sampling of spline fits to the data of **a** (measured by coherent shuttling). **f** Histogram of the measured E_{ST} using all data from **d** (measured by magnetospectroscopy). Both datasets are plotted with a maximum-likelihood fitted Rician distribution (solid line) and folded Gaussian distribution (black, dashed line).

Comparison to magnetospectroscopy

In order to benchmark our method for mapping the local E_{VS} by shuttling, we measure another map using the well-established method of magnetospectroscopy. We employ a device with the same heterostructure, gate geometry, and fabrication process, but the 1DEC is half in length and nine (instead of 17) individually tuneable (i.e., not interconnected) clavier gates are fabricated on top of the 1DEC (SEM is shown in the Supplementary Fig. 6a). We form a single QD at a time in the 1DEC by biasing some clavier gates and by the voltages V_{ST}, V_{SB} applied to the long split-gate. To conduct the magnetospectroscopy, we tunnel-couple the QD to an accumulated electron reservoir reaching out to one SET, while the closer SET detects the charge state of the QD (see Supplementary Note VII for all details). We repeat the magnetospectroscopy each time, forming a single QD at a different position in the 1DEC. The locations of these QDs (Fig. 4d) are determined by triangulation with the QD's capacitive coupling to its four surrounding gates, and by a finite-element Poisson solver of the full device (see Supplementary Note VII). The orbital splitting E_{orb} of each QD is measured by pulsed-gate spectroscopy yielding values in the range E_{orb} ~1.4−3.6 meV. By magnetospectroscopy, the two-electron singlet-triplet energy splitting E_{ST} of the shaped QD can be directly measured. We nevertheless assume E_{VS} ~E_{ST} to be a reasonable estimate, as the ratio between the two has been measured to be $E_{\mathrm{ST}}/E_{\mathrm{V\,S}} \lesssim 1$[24], if $E_{\mathrm{orb}} \gg E_{\mathrm{VS}}$ with E_{VS} then being weakly dependent on E_{orb}[46].

This assumption allows comparing the histograms of both 2D maps (conveyor-mode shuttling in Fig. 4e and magnetospectroscopy in Fig. 4f). Assuming that E_{VS} and E_{ST} are both governed by alloy disorder, their distributions are expected to be Rician[12,31,47]

$$f(x \mid \gamma, \sigma) = \frac{x}{\sigma^2}\exp\left(-\frac{x^2+\gamma^2}{2\sigma^2}\right) I_0\left(\frac{x\gamma}{\sigma^2}\right). \qquad (4)$$

$I_0(x)$ is the modified Bessel function of the first kind and order zero. γ is the non-centrality parameter and σ the scaling parameter. The fitted parameters γ and σ for both distributions (Table 2) are very similar. The σ parameter expressing the randomness of the parameters is equal within the error range. The γ parameter for E_{ST} is a bit lower than the one of E_{VS} as expected. This all strongly supports the validity of our shuttle-based method for mapping the valley splittings.

Table 2 | Parameters fitting the distributions

Parameter	value (CS)	1σ (CS)	value (MS)	1σ (MS)
γ	35.4 µeV	0.6 µeV	29.6 µeV	5.9 µeV
σ	13.6 µeV	0.4 µeV	14.2 µeV	3.6 µeV
μ	38.1 µeV	0.5 µeV	33.2 µeV	2.3 µeV
$\tilde{\sigma}$	13.0 µeV	0.3 µeV	13.1 µeV	1.8 µeV

In this table, we summarize the fit parameters that yield the fits in Fig. 4e for coherent shuttling (CS) and Fig. 4f for magnetospectroscopy (MS) with standard deviation 1σ.

Intriguingly, we observe that $\gamma > \sigma$. Consequently, both histograms can be well-fitted by modified Gaussians (dashed lines in Fig. 4e, f):

$$f(x\,|\,\mu,\tilde{\sigma}) = \frac{1}{\sqrt{2\pi\tilde{\sigma}^2}} \times \left(\exp\left\{\left(-\frac{(x-\mu)^2}{2\tilde{\sigma}^2}\right)\right\} + \exp\left\{\left(-\frac{(x+\mu)^2}{2\tilde{\sigma}^2}\right)\right\}\right), \tag{5}$$

with fitted parameters summarized in Table 2. This indicates that for both E_{VS} and E_{ST} the randomness due to SiGe alloy disorder does not dominate over the deterministic contribution given by γ[12,31,47]. However, care must be taken for the analysis of the histograms presented here, since a larger number of uncorrelated E_{VS} samples are required to reduce the error of the Gaussian tails. The samples for both histograms contain multiple points that are spatially closer than the fitted correlation length in Fig. 4c. In addition, both histograms are slightly biased by omitting potentially a few small values due to the non-valid $E_{\mathrm{VS}}(d)$ in Fig. 4a. Especially, obtaining E_{ST} smaller than the electron temperature by magnetospectroscopy is challenging and might explain that all $E_{\mathrm{ST}} > 12$ μeV. In comparison, detecting E_{VS} lower than the electron temperature is possible by conveyor-mode shuttling.

Discussion

We introduced a method for 2D mapping of the valley splitting E_{VS} in a Si/SiGe SQS with sub-μeV energy accuracy and nanometer lateral resolution. The method is based on the separation and rejoining of spin-entangled electron pairs by conveyor-mode shuttling. Spin-singlet-triplet oscillations serve as a probe to identify spin-valley anticrossings and to extract the E_{VS} of both a static and a shuttled electron. The nanometer-fine tunability of the position of the shuttled QD allows for dense measurements, which allows us to identify local variations of the valley-splitting landscape. By DC biasing the screening gates confining the 1DEC, we record a two-dimensional map of a large area. The method requires devices very similar to the ones used for quantum computation. Thus, the method is easily applicable and captures typical influences on the valley splitting e.g., effects from device fabrication. In principle, shuttling a single electron spin set in a spin superposition is sufficient for our method.

We benchmarked our results with magnetospectroscopy measurements—a well-established measurement method—on the same heterostructure and found the distributions of the measured map of singlet-triplet splittings to agree very well with the developed method. Note that mapping by magnetospectroscopy is limited in range due to the need for a proximate charge detector, and that the pure recording time required to obtain the presented 2D E_{ST} map took us ~100 times longer than the more detailed E_{VS} map obtained by conveyor-mode shuttling. While the extent of the latter map is spatially limited due to electrostatic disorder, we expect that higher confinement (large signal voltages) of the propagating QD will allow us to extend the mapped region until we reach fundamental limitations due to spin-dephasing, which is enhanced by shuttling across the E_{VS}-hotspots[11]. This method offers a more comprehensive approach to heterostructure characterization and exploration, potentially aiding advancements in heterostructure growth and valley-splitting engineering. Our results highlight the immediate benefits of conveyor-mode spin-coherent shuttling, not only for scaling up quantum computing systems but also for efficient material parameter analysis. Finally, the valley splitting map of a specific shuttle device allows for optimization of its spin-shuttling strategy[48].

Methods

Shuttle pulses

In this section, we explain conveyor-mode electron shuttling in the 1DEC[39–41,43]. During the pulse stages T, d, and again T of the experiment, we apply sinusoidal pulses $V_{\mathrm{S},i}$ on the shuttle gates Si (S1–S4):

$$V_{\mathrm{S},i}(\tau_{\mathrm{S}}) = U_i \cdot \sin(2\pi f \tau_{\mathrm{S}} + \varphi_i) + C_i. \tag{6}$$

The amplitudes (U_1, U_3) applied to the gate sets S1 and S3 on the second layer (blue in Fig. 1a) is $U_{\mathrm{lower}} = 150$ mV, whereas the amplitudes (U_1, U_3) applied to the gate sets S2 and S4 on the 3rd metal layer is slightly higher ($U_{\mathrm{upper}} = 1.28 \cdot U_{\mathrm{lower}} = 192$ mV) to compensate for the difference of capacitive coupling of these layers to the quantum well[41]. This compensation extends to the DC-part of the shuttle gate voltages. The offsets $C_1 = C_3 = 0.7$ V are chosen to form a smooth DQD, whilst $C_2 = C_4 = 0.896$ V are chosen to form a smooth DC potential. The phases are chosen in order to build a traveling wave potential across the one-dimensional electron channel ($\varphi_1 = -\pi/2$, $\varphi_2 = 0$, $\varphi_3 = \pi/2$, $\varphi_4 = \pi$) with wavelength $\lambda = 280$ nm. The frequency f is set to 10 MHz resulting in a nominal shuttle velocity of 2.8 ms^{-1}. The nominal shuttling distance d relates to the assumption that the electron travels at a constant velocity $\lambda \cdot f$[41]. Deviations from this nominal shuttling distance by potential disorder or strain are possible[49].

Retuning SET and PSB

In order to compensate for slow charge-noise drifts on the PSB and the SET, both the PSB-stage voltage as well as the SET voltages are retuned after 1000 repetitions. For this, we track the spin fractions as well as the readout threshold between the charge configurations for singlet (4,0) and triplet (3,1). If we detect a significant change (~10%) in spin fractions, this means the PSB region drifted, and a correction via the G2 DC voltage is done. Similarly, a significant change in the readout threshold indicates a drift of the Coulomb peak on the SET, resulting in the need to adjust its plunger voltage accordingly.

Layer stack of the used heterostructure

The used Si/SiGe heterostructure is grown by chemical vapor deposition and has the following layer stack according to specification (top-to-bottom): Si-cap (2 nm), $\mathrm{Si}_{0.7}\mathrm{Ge}_{0.3}$ spacer (30 nm), strained Si quantum well (10 nm), $\mathrm{Si}_{0.7}\mathrm{Ge}_{0.3}$ barrier on virtual SiGe substrate.

Data availability

The data that supports the findings of this study are available in the Zenodo repository (https://doi.org/10.5281/zenodo.10359903).

Received: 29 December 2023; Accepted: 17 May 2024;
Published online: 19 June 2024

References

1. Stano, P. & Loss, D. Review of performance metrics of spin qubits in gated semiconducting nanostructures. *Nat. Rev. Phys.* **4**, 672 (2022).
2. Struck, T. et al. Low-frequency spin qubit energy splitting noise in highly purified ^{28}Si/SiGe. *npj Quantum Inf.* **6**, 2056 (2020).
3. Yoneda, J. et al. A quantum-dot spin qubit with coherence limited by charge noise and fidelity higher than 99.9%. *Nat. Nanotechnol.* **13**, 102 (2018).
4. Xue, X. et al. Quantum logic with spin qubits crossing the surface code threshold. *Nature* **601**, 343 (2022).
5. Noiri, A. et al. Fast universal quantum gate above the fault-tolerance threshold in silicon. *Nature* **601**, 338 (2022).
6. Mills, A. R. et al. Two-qubit silicon quantum processor with operation fidelity exceeding 99%. *Sci. Adv.* **8**, eabn5130 (2022).
7. Neyens, S. et al. Probing single electrons across 300 mm spin qubit wafers. *Nature* **629**, 80–85 (2024).
8. Kawakami, E. et al. Electrical control of a long-lived spin qubit in a Si/SiGe quantum dot. *Nat. Nanotechnol.* **9**, 666 (2014).
9. Vandersypen, L. M. K. et al. Interfacing spin qubits in quantum dots and donors—hot, dense, and coherent. *npj Quantum Inf.* **3**, 34 (2017).
10. Ferdous, R. et al. Valley dependent anisotropic spin splitting in silicon quantum dots. *npj Quantum Inf.* **4**, 26 (2018).

11. Langrock, V. et al. Blueprint of a scalable spin qubit shuttle device for coherent mid-range qubit transfer in disordered Si/SiGe/SiO$_2$. *PRX Quantum* **4**, 020305 (2023).
12. Losert, M. P. et al. Practical strategies for enhancing the valley splitting in Si/SiGe quantum wells. *Phys. Rev. B* **108**, 125405 (2023).
13. Woods, B. D. et al. Coupling conduction-band valleys in modulated SiGe heterostructures via shear strain. *npj Quantum Inf.* **10**, 54 (2024).
14. Neul, M. et al. Local laser-induced solid-phase recrystallization of phosphorus-implanted Si/SiGe heterostructures for contacts below 4.2 K. *Phys. Rev. Mater.* **8**, 043801 (2024).
15. Borselli, M. G. et al. Measurement of valley splitting in high-symmetry Si/SiGe quantum dots. *Appl. Phys. Lett.* **98**, 123118 (2011).
16. Shi, Z. et al. Tunable singlet-triplet splitting in a few-electron Si/SiGe quantum dot. *Appl. Phys. Lett.* **99**, 233108 (2011).
17. Zajac, D. M., Hazard, T. M., Mi, X., Wang, K. & Petta, J. R. A reconfigurable gate architecture for Si/SiGe quantum dots. *Appl. Phys. Lett.* **106**, 223507 (2015).
18. Mi, X., Péterfalvi, C. G., Burkard, G. & Petta, J. R. High-resolution valley spectroscopy of Si quantum dots. *Phys. Rev. Lett.* **119**, 176803 (2017).
19. Jones, A. et al. Spin-blockade spectroscopy of Si/Si-Ge quantum dots. *Phys. Rev. Appl.* **12**, 014026 (2019).
20. Borjans, F., Zajac, D. M., Hazard, T. M. & Petta, J. R. Single-spin relaxation in a synthetic spin-orbit field. *Phys. Rev. Appl.* **11**, 044063 (2019).
21. Hollmann, A. et al. Large, tunable valley splitting and single-spin relaxation mechanisms in a Si/Si$_x$Ge$_{1-x}$ quantum dot. *Phys. Rev. Appl.* **13**, 034068 (2020).
22. McJunkin, T. et al. Valley splittings in Si/SiGe quantum dots with a germanium spike in the silicon well. *Phys. Rev. B* **104**, 085406 (2021).
23. Chen, E. H. et al. Detuning axis pulsed spectroscopy of valley-orbital states in Si/Si-Ge quantum dots. *Phys. Rev. Appl.* **15**, 044033 (2021).
24. Dodson, J. P. et al. How valley-orbit states in silicon quantum dots probe quantum well interfaces. *Phys. Rev. Lett.* **128**, 146802 (2022).
25. Denisov, A. O. et al. Microwave-frequency scanning gate microscopy of a Si/SiGe double quantum dot. *Nano Lett.* **22**, 4807 (2022).
26. Degli Esposti, D. et al. Low disorder and high valley splitting in silicon. *npj Quantum Inf.* **10**, 32 (2024).
27. Friesen, M., Chutia, S., Tahan, C. & Coppersmith, S. N. Valley splitting theory of SiGe/Si/SiGe quantum wells. *Phys. Rev. B* **75**, 115318 (2007).
28. Friesen, M. & Coppersmith, S. N. Theory of valley-orbit coupling in a Si/SiGe quantum dot. *Phys. Rev. B* **81**, 115324 (2010).
29. Culcer, D., Hu, X. & Das Sarma, S. Interface roughness, valley-orbit coupling, and valley manipulation in quantum dots. *Phys. Rev. B* **82**, 205315 (2010).
30. Hosseinkhani, A. & Burkard, G. Electromagnetic control of valley splitting in ideal and disordered Si quantum dots. *Phys. Rev. Res.* **2**, 043180 (2020).
31. Paquelet Wuetz, B. et al. Atomic fluctuations lifting the energy degeneracy in Si/SiGe quantum dots. *Nat. Commun.* **13**, 7730 (2022).
32. Liu, Y.-Y. et al. Magnetic-gradient-free two-axis control of a valley spin qubit in Si$_x$Ge$_{1-x}$. *Phys. Rev. Appl.* **16**, 024029 (2021).
33. Cai, X., Connors, E. J., Edge, L. F. & Nichol, J. M. Coherent spin-valley oscillations in silicon. *Nat. Phys.* **19**, 386 (2023).
34. Burkard, G. & Petta, J. R. Dispersive readout of valley splittings in cavity-coupled silicon quantum dots. *Phys. Rev. B* **94**, 195395 (2016).
35. Mi, X. et al. Magnetotransport studies of mobility limiting mechanisms in undoped Si/SiGe heterostructures. *Phys. Rev. B* **92**, 035304 (2015).
36. Paquelet Wuetz, B. et al. Effect of quantum hall edge strips on valley splitting in silicon quantum wells. *Phys. Rev. Lett.* **125**, 186801 (2020).
37. Friesen, M., Eriksson, M. A. & Coppersmith, S. N. Magnetic field dependence of valley splitting in realistic Si/SiGe quantum wells. *Appl. Phys. Lett.* **89**, 202106 (2006).
38. Jock, R. M. et al. A silicon singlet-triplet qubit driven by spin-valley coupling. *Nat. Commun.* **13**, 641 (2022).
39. Seidler, I. et al. Conveyor-mode single-electron shuttling in Si/SiGe for a scalable quantum computing architecture. *npj Quantum Inf.* **8**, 100 (2022).
40. Xue, R. et al. Si/SiGe QuBus for single electron information-processing devices with memory and micron-scale connectivity function. *Nat. Commun.* **15**, 2296 (2024).
41. Struck, T. et al. Spin-EPR-pair separation by conveyor-mode single electron shuttling in Si/SiGe. *Nat. Commun.* **15**, 1325 (2024).
42. We use the same naming convention as in refs. [4, 11, 39, 41], where an SQS shuttles a single-spin qubit and a quantum bus (QuBus) shuttles a quantized charge.
43. Künne, M. et al. The SpinBus architecture for scaling spin qubits with electron shuttling. *Nat. Commun.* **15**, 4977 (2024).
44. Nurizzo, M. et al. Complete readout of two-electron spin states in a double quantum dot. *PRX Quantum* **4**, 010329 (2023).
45. Connors, E. J., Nelson, J., Edge, L. F. & Nichol, J. M. Charge-noise spectroscopy of Si/SiGe quantum dots via dynamically-decoupled exchange oscillations. *Nat. Commun.* **13**, 940 (2022).
46. Ercan, H. E., Coppersmith, S. N. & Friesen, M. Strong electron-electron interactions in Si/SiGe quantum dots. *Phys. Rev. B* **104**, 235302 (2021).
47. Lima, J. R. F. & Burkard, G. Valley splitting depending on the size and location of a silicon quantum dot. *Phys. Rev. Mater.* **8**, 036202 (2024).
48. Losert, M. et al. Strategies for enhancing spin-shuttling fidelities in Si/SiGe quantum wells with random-alloy disorder. Preprint at https://arxiv.org/abs/2405.01832 (2024).
49. Corley-Wiciak, C. et al. Lattice deformation at submicron scale: X-ray nanobeam measurements of elastic strain in electron shuttling devices. *Phys. Rev. Appl.* **20**, 024056 (2023).
50. Albrecht, W., Moers, J. & Hermanns, B. HNF—helmholtz nano facility. *J. Large Scale Res. Facil. (JLSRF)* **3**, A112 (2017).

Acknowledgements

We acknowledge valuable discussions with Merritt P. Losert and Mark Friesen and the support of the Dresden High Magnetic Field Laboratory (HLD) at the Helmholtz-Zentrum Dresden—Rossendorf (HZDR), a member of the European Magnetic Field Laboratory (EMFL). This work was funded by the German Research Foundation (DFG) within the project 421769186 (SCHR 1404/5-1) and under Germany's Excellence Strategy—Cluster of Excellence Matter and Light for Quantum Computing" (ML4Q) EXC 2004/1—390534769 and by the Federal Ministry of Education and Research under Contract no. FKZ: 13N14778, and by the National Science Center (NCN), Poland, under QuantERA program, Grant no. 2017/25/Z/ST3/03044. Project Si-QuBus received funding from the QuantERA ERA-NET CoFund in Quantum Technologies implemented within the European Union's Horizon 2020 Program. The device fabrication has been done at HNF—Helmholtz Nano Facility, Research Center Juelich GmbH[50].

Author contributions

M.V. and T.S. contributed equally to this work. M.V., T.S., and B.C. set up and conducted the experiments assisted by L.V. Authors M.V., T.S., A.S., B.C., T.O., Ł.C., and L.R.S. analyzed the data supported by M.O. Device fabrication was done by J.T., R.X., and S.T. Author L.R.S. designed and supervised the experiment. L.R.S. and H.B. provided guidance to all authors. M.V., T.S., A.S., and L.R.S. wrote the manuscript, which was commented on by all other authors.

Funding

Open Access funding enabled and organized by Projekt DEAL.

Competing interests

The method for mapping valley splitting in a semiconductor device is covered by a patent registration (PCT/EP2023/077176) by inventors L.R.S., T.S., H.B., and M.V. The patent application, co-owned by applicants RWTH Aachen University and the Forschungszentrum Jülich, is currently pending.

L.R.S. and H.B. are founders and shareholders of ARQUE Systems GmbH. The remaining authors declare no competing interest.

Additional information

Supplementary information The online version contains supplementary material available at https://doi.org/10.1038/s41534-024-00852-7.

Correspondence and requests for materials should be addressed to Lars R. Schreiber.